fluids

MDPI

Article

Impact of Porous Media on Boundary Layer Turbulence

Sutharsan Satcunanathan [1,*], Matthias Meinke [1,2] and Wolfgang Schröder [1,2]

[1] Institute of Aerodynamics, RWTH Aachen University, Wüllnerstr. 5a, 52062 Aachen, Germany; m.meinke@aia.rwth-aachen.de (M.M.); office@aia.rwth-aachen.de (W.S.)
[2] JARA Centre for Simulation and Data Science, RWTH Aachen University, Seffenter Weg 23, 52074 Aachen, Germany
* Correspondence: s.satcunanathan@aia.rwth-aachen.de; Tel.: +49-241-8095410

Abstract: The subsonic flows around NACA 0012 aerofoils with a solid, a porous, and a poro-serrated trailing edge (TE) at a Reynolds number of 1×10^6 are investigated by a hybrid Reynolds-averaged Navier–Stokes (RANS)/large-eddy simulation (LES) approach. The porosity is treated by the method-of-volume averaging. In the RANS, a two-equation low Reynolds number k-ε turbulence model is modified to include the porous treatment. Similarly the equations in the LES are extended by the Darcy–Forchheimer model. The simulation is set up with the broadband turbulent boundary layer trailing edge (TBL-TE) noise prediction as a future objective in mind, i.e., the noise sources in the trailing edge region are captured by the LES. To enforce a physically realistic transition from an averaged RANS solution towards a resolved turbulent flow field, at the inflow of the LES coherent structures are generated by means of the reformulated synthetic turbulence generation (RSTG) method. For the poro-serrated TE, turbulence statistics vary in the spanwise direction between the two extremes of a pure solid and a rectangular porous TE, where porosity locally increases the level of turbulence intensity and alters the near wall turbulence anisotropy.

Keywords: porous media; turbulent boundary layer; large eddy simulation

check for updates

Citation: Satcunanathan, S.; Meinke, M.; Schröder, W. Impact of Porous Media on Boundary Layer Turbulence. *Fluids* **2022**, *7*, 139. https://doi.org/10.3390/fluids7040139

Academic Editor: Martin Skote

Received: 1 March 2022
Accepted: 8 April 2022
Published: 13 April 2022

Publisher's Note: MDPI stays neutral with regard to jurisdictional claims in published maps and institutional affiliations.

Copyright: © 2022 by the authors. Licensee MDPI, Basel, Switzerland. This article is an open access article distributed under the terms and conditions of the Creative Commons Attribution (CC BY) license (https://creativecommons.org/licenses/by/4.0/).

1. Introduction

Experimental and numerical investigations confirm that porous surface treatments are a promising technique to mitigate airframe noise generated by leading or trailing edges [1–3]. The permeable surface changes the pressure field, acoustic impedance, and also the near wall turbulence in comparison to a solid surface. The focus in this paper is on the analysis of the alteration of the boundary layer turbulence caused by a porous surface installed at the trailing edge of an aerofoil. Previous investigations of turbulence interacting with porous media have been conducted, e.g., in [4] for a turbulent wake generated by an upstream cylinder impinging on a thick aerofoil made of porous material. The results obtained with large-eddy simulations showed that the porosity reduces the amplitude of pressure oscillations, which is localised in the low-frequency range of the spectrum. The porous medium is responsible for a milder distortion of the incoming vortices, but is not capable of breaking the spanwise coherence or in-phase behaviour of the surface-pressure fluctuations at the vortex-shedding frequency. The Reynolds-stress term possesses a considerable strength in the stagnation region of the aerofoil, where the wall normal velocity is larger and is partly correlated with the unsteady surface pressures.

In [5], trailing edge noise from a blunt trailing edge, exhibiting a tonal peak in the acoustic spectrum caused by a turbulent vortex shedding, was investigated. A parametric study of the flow and acoustic fields of various shaped blunt trailing edges with different porous media parameters was conducted. For an aerodynamic and acoustic evaluation, the skin friction and the surface resistance to quantify the acoustic impedance were determined. Recommendations concerning the range of values of the two major parameters

characterising a porous material, i.e., the porosity and the pore size, for noise reduction, were given.

Unlike the previous work, the turbulent flow is analysed in this study for a sharp solid, porous, and poro-serrated trailing edge of an NACA-0012 aerofoil to avoid tonal acoustic wave components. The main objective is to understand the impact of the porosity on the boundary layer turbulence, which is important for a better understanding of the trailing edge noise mitigation effect. The analysis is based on wall resolved large-eddy simulations (LES) conducted for typical wind tunnel Reynolds numbers. One way to predict the flow through a porous medium would be to perform a spatially fully resolved simulation of the porous micro-structures without a porous media modelling. Such a fully resolved porous material simulation, however, is at present only possible for simple validation or benchmark tests. Due to the large disparity of length scales in realistic technical applications with porous media, the computational effort becomes too large. Therefore, it is common to utilise the method of volume-averaging [6], which assumes a separation of scales between the pores and the flow features of interest. Compared to a direct pore structure resolving simulation, it enables the efficient prediction of the integral effects of the porous material. The air-saturated porous medium is treated as a homogeneous phase with spatially filtered continuously varying field variables in space and time, which are governed by the volume-averaged Navier–Stokes equations (VANS). This constitutes a closure problem, where the impact of the microscopic scales is substituted by surface filter terms, which need to be modelled. Such porous media models have been presented in [7,8] for LES and, e.g., in [9] for the Reynolds averaged Navier–Stokes equations (RANS), which are also used in this paper.

The structure of this paper is as follows. First, the mathematical formulation of the governing equations used for the predictions based on the RANS and the LES for porous media are presented and the zonal coupling strategy is outlined. The numerical method, i.e., the discretisation and time integration is described next. Then, the numerical setup is defined and the results for a solid, porous, and poro-serrated trailing edge are presented. Finally, the findings are summarised and discussed in the conclusion.

2. Mathematical Model

The turbulent flow field is predicted by an LES of a compressible fluid. The Navier–Stokes equations are equally valid inside the porous material and can be employed to fully resolve the flow through the porous micro-structures, which is difficult for various reasons. On the one hand, this requires the complex pore morphology to be available, e.g., from a computer tomography scan, which is not always the case. On the other hand, the requirement on the grid resolution would be severe due to the tiny pore structures being typically orders of magnitude smaller than an integral length scale of the flow problem such as the chord length of an aerofoil. Often, only the integral effects or the flow alterations in the outer region by a porous treatment are of interest. A well-established approach is to neglect the micro-scale introduced by the pores of the material by the method of volume averaging [6,10]. This procedure replaces the distinct fluid and solid regions in the porous material with a locally homogeneous medium with continuously varying field variables. These are governed by the VANS augmented by closure terms, which emerge from the spatial filtering process and account for sub-grid effects. For more details, the reader is referred to Satcunanathan et al. [8]. The following presentation of the equations solved in the LES and RANS closely follows previous works by the authors [4,11] and they are included here for completeness.

In the subsequent brief consideration, let Ω be the total simulation domain, $\Omega_f = \{\underline{x} \in \Omega \mid \varphi(\underline{x}) = 1\}$ the fluid region, $\Omega_p = \{\underline{x} \in \Omega \mid \varphi(\underline{x}) < 1\}$ the porous region with $\Omega_g \cap \Omega_p = \emptyset$, and $\Gamma = \partial\Omega_f \cap \Omega_p$ the fluid–porous interface. The porosity φ is the volume ratio of the open pores to the total volume of the porous material, and is equal to 1 in the free fluid. Using the symbol $\langle\,\rangle$ to denote the intrinsic average and $\langle\,\rangle_F$ to denote the Favre

average, the conservation of mass, momentum, and energy in non-dimensional integral form formulated for an arbitrary control volume V reads:

$$\frac{\mathrm{d}}{\mathrm{d}t}\int\limits_{V\in\Omega}\underline{Q}\,\mathrm{d}V+\oint\limits_{\partial V\in\Omega}\left(\underline{\underline{H}}^{\mathrm{inv}}-\underline{\underline{H}}^{\mathrm{vis}}\right)\cdot\underline{n}\,\mathrm{d}S+\int\limits_{V\in\Omega}\left(\frac{1}{\varphi}\underline{\underline{H}}^{\mathrm{inv}}\cdot\nabla\varphi+\underline{S}\right)\mathrm{d}V=0, \tag{1}$$

where $\underline{Q}=\left[\langle\rho\rangle,\langle\rho\rangle\langle\underline{u}\rangle_F,\langle\rho\rangle\langle E\rangle_F\right]^T$ is the vector of spatially-averaged conservative variables. The inviscid and viscous fluxes are given by:

$$\underline{\underline{H}}^{\mathrm{inv}}-\underline{\underline{H}}^{\mathrm{vis}}=\begin{bmatrix}\langle\rho\rangle\langle\underline{u}\rangle_F\\ \langle\rho\rangle\langle\underline{u}\rangle_F\otimes\langle\underline{u}\rangle_F+\langle p\rangle\underline{\underline{I}}\\ \langle\rho\rangle\langle E\rangle_F\langle\underline{u}\rangle_F+\langle p\rangle\langle\underline{u}\rangle_F\end{bmatrix}-\frac{1}{Re}\begin{bmatrix}0\\ \langle\underline{\underline{\tau}}\rangle_F\\ \langle\underline{\underline{\tau}}\rangle_F\cdot\langle\underline{u}\rangle_F+\frac{1}{Pr}\langle\underline{q}\rangle\end{bmatrix}. \tag{2}$$

The quantities E, $\underline{q}$, $\underline{\underline{I}}$, Re, and Pr denote the total energy, heat-flux vector, unit tensor, Reynolds number, and Prandtl number. The first two integrals in Equation (1) are formally identical to the equations solved in a monotone integrated LES (MILES) context for $\varphi=1$, where no explicit modelling of the sub-grid scale is used. The first term in the last integral is the contribution of the inviscid flux vector at the fluid–porous interface $\underline{\underline{H}}^{\mathrm{int}}=\underline{\underline{H}}^{\mathrm{inv}}-\langle p\rangle\underline{\underline{I}}$. The surface-filter term,

$$\underline{\underline{S}}=\begin{cases}[0,\underline{F}/\varphi,0]^T, & \underline{x}\in\Omega_p\\ \underline{0}^T, & \underline{x}\in\Omega_f,\end{cases} \tag{3}$$

contains the porous drag vector $\underline{F}$ that is closed through the Darcy–Forchheimer model [12,13], expressed for a homogeneous and isotropic porous medium as:

$$\underline{F}=\underbrace{\frac{1}{Re_k\sqrt{Da}}\varphi\mu\langle\underline{u}\rangle_F}_{\text{Darcy}}+\underbrace{\frac{1}{\sqrt{Da}}\varphi^2c_f\langle\rho\rangle|\langle\underline{u}\rangle_F|\langle\underline{u}\rangle_F}_{\text{Forchheimer}}. \tag{4}$$

The permeability Reynolds number, $Re_k=Re\sqrt{Da}$, is computed with $d_p\sim\sqrt{k}$ as the length scale, which is a measure for the effective pore diameter, while the Darcy number, Da, is defined as $Da=k/L^2$, L being a reference length. The Darcy–Forchheimer model in Equation (4), together with Equation (1), characterises the porous medium in terms of the porosity, φ, static permeability, k, and Forchheimer coefficient, c_F, and assumes the porous frame to be rigid, neglecting coupling effects due to elasticity as well as thermal effects.

The RANS equations in free fluid are obtained by Reynolds averaging the Navier–Stokes equations. In the presence of porous media, however, there is no agreement on whether to apply volume-averaging first followed by Reynolds averaging or vice versa. It is argued that Reynolds averaging first will preserve microscale turbulence. Here, we adopt the formulation by Mößner et al. [9], who use volume-averaging before Reynolds averaging, which they justify by the results of Breugem [14], who obtained a good match between a volume averaged DNS and a geometry resolved DNS of a generic porous channel flow.

The Reynolds averaging of Equations (1)–(4) will result in a closure problem for the Reynolds stresses because of the non-linearity of the inertia terms. We choose to use the low Reynolds number k-ε model by Chien [15]. The advantage of using the (isotropic) rate of dissipation ε as the second turbulence variable over the other two-equation models is the fact that equations for the turbulent kinetic energy k, ε or the Reynolds stresses can be derived by analytical manipulations of the Navier–Stokes equations and therefore starting from the Equations (1)–(4), model terms for k and ε can be derived. The additional terms for the porous media are adopted from Mößner et al. [9], who proposed the modifications for a Reynolds stress model. The closure in Equation (4) becomes:

$$\mathcal{F}_i=\frac{\varphi\mu\tilde{u}_i}{Re_{d_p}\sqrt{Da}}+\frac{\varphi^2c_F\bar{\rho}}{\sqrt{Da}}\left(|\tilde{u}|\tilde{u}_i+\frac{k}{|\tilde{u}|}\tilde{u}_i+\frac{\tilde{u}_j}{|\tilde{u}|}\widetilde{u_i'u_j'}-\frac{1}{2}\frac{\tilde{u}_i\tilde{u}_j\tilde{u}_k}{|\tilde{u}|^3}\widetilde{u_j'u_k'}\right), \tag{5}$$

where $\bar{(\,)}$ denotes Reynolds averaging, $\tilde{(\,)}$ denotes Favre averaging and $(\,)' = (\,) - \tilde{(\,)}$. The porous terms in the k-equation are obtained by taking half the contraction of the model terms in the Reynolds stress model. The non-dimensional transport equations for k and ε read:

$$\frac{\partial \rho u_j k}{\partial x_j} = \frac{1}{Re}\frac{\partial \mu_k \frac{\partial k}{\partial x_j}}{\partial x_j} + P - \rho\varepsilon(1+M_t^2) - \frac{1}{Re}\frac{2\mu k}{y_w^2} + \mathcal{D}_k - \mathcal{P}_k \tag{6}$$

$$\frac{\partial \rho u_j \varepsilon}{\partial x_j} = \frac{1}{Re}\frac{\partial \mu_\varepsilon \frac{\partial \varepsilon}{\partial x_j}}{\partial x_j} + c_1\frac{\varepsilon}{k}P - \frac{\varepsilon}{k}\left(c_2 f_2 \rho\varepsilon + \frac{1}{Re}\frac{2\mu k e^{-c_4 y_w^+}}{y_w^2}\right) - \mathcal{P}_\varepsilon\,, \tag{7}$$

where P is the classical production term, $\mu_k = \mu + \mu_t/\sigma_k$ and $\mu_\varepsilon = \mu + \mu_t/\sigma_\varepsilon$ with σ_k and σ_ε being the turbulent Prandtl numbers, the compressibility correction $M_t^2 = 1.5k/a^2$ with a the speed of sound, y_w (y_w^+) the distance to the wall (in viscous units), and $\mathcal{D}$, $\mathcal{P}_k$, and $\mathcal{P}_\varepsilon$ the porous model terms. The turbulent eddy viscosity is computed from $\mu_t = c_\mu f_\mu \rho k^2/\varepsilon$. The auxiliary functions are $f_2 = 1 - \frac{0.4}{1.8}e^{-Re_T^2/36}$ and $f_\mu = 1 - e^{-c_3 y_w^+}$ with $Re_T = \rho k^2/\mu\varepsilon$. An additional diffusion term,

$$\mathcal{D} = \frac{\partial}{\partial x_j}\left(c_{D,p,eff}\frac{k^2}{\varepsilon}\frac{\partial k}{\partial x_j}\right), \tag{8}$$

was added inside the porous media, where $c_{D,p,eff} \in [0, c_{D,p})$ depends on a smooth indicator function as given in [9] and was argued to be necessary for low permeability materials only. The porous terms in Equations (6) and (7) are:

$$\mathcal{P}_k = \frac{2\varphi\mu k}{Re_{d_p}\sqrt{Da}} + \frac{\varphi^2 c_F \bar{\rho}}{2\sqrt{Da}}\left(4k|\tilde{u}| + 2\frac{\tilde{u}_i\tilde{u}_k}{|\tilde{u}|}\widetilde{u_i'u_k'} + 3\frac{\tilde{u}_k}{|\tilde{u}|}\widetilde{u_i'u_i'u_k'} - \frac{\tilde{u}_i\tilde{u}_m\tilde{u}_k}{|\tilde{u}|^3}\widetilde{u_i'u_m'u_k'}\right) \tag{9}$$

$$\mathcal{P}_\varepsilon = \frac{2\varphi\mu\varepsilon}{Re_{d_p}\sqrt{Da}} + \frac{\varphi^2 c_F \bar{\rho}}{\sqrt{Da}}\left(\frac{8}{3}|\tilde{u}|\varepsilon + \frac{2\nu}{Re}\frac{\partial|\tilde{u}|}{\partial x_j}\frac{\partial k}{\partial x_j} - 2c_\varepsilon\frac{k}{\varepsilon}\frac{\tilde{u}_k}{|\tilde{u}|}\widetilde{u_k'u_i'}\frac{\partial \varepsilon}{\partial x_i} + \frac{\nu}{Re}\frac{\partial}{\partial x_j}\left(\frac{\tilde{u}_i\tilde{u}_k}{|\tilde{u}|}\frac{\partial\widetilde{u_i'u_k'}}{\partial x_j}\right)\right). \tag{10}$$

In [9], a standard parameter set was given for the use of the terms in their Reynolds stress model, where some parameters were set to zero due to a lack of reference data for calibration. This includes the triple correlation, such that here this term will also not be taken into account either. Low Reynolds number models incorporate the wall distance to express a near wall damping effect. At a fluid–porous interface, these distances are modified to account for the relaxed blocking effect compared to a solid wall as also suggested in [9]. Values for all remaining constants can be found in the original publications. For the turbulence quantities k and ε, additional interface conditions need to be prescribed.

3. Numerical Method

Equation (1) is discretised by a finite-volume method, in which the advective upstream splitting method (AUSM) is used to formulate the inviscid fluxes on the cell surfaces. For the viscous fluxes, a central discretisation is used. The discrete approximation is based on a locally refined, unstructured, hierarchical Cartesian mesh with a fully conservative cut-cell approach for the wall boundaries [16]. The spatially discretised equations are advanced in time by a low-storage [17] five-stage explicit Runge–Kutta scheme, which is optimised for stability. The overall scheme is second-order accurate in space and time. For LES, the subgrid scales are modelled by the MILES ansatz.

Equation (1) is valid in the pure fluid and pure porous regions, but assumptions made during the derivation are violated across the fluid–porous interface Γ. Additionally, the sudden change of φ across Γ makes the equations stiff. It can be shown that the arising

Dirac-shaped source terms can be equally replaced by jumps of the flow variables across an idealised sharp immersed fluid–porous interface on a non-interface fitted Cartesian mesh. In such a fluid–porous cut cell, the volume-weighted average of the state vector $\underline{Q} = \varphi\ \underline{Q}_f + (1-\varphi)\ \underline{Q}_p$ is integrated in time, preventing the emergence of small cells, which may pose stringent time-step constraints. In this case, the flow variables on the porous surface correspond to $\underline{Q}_f$ of the respective cut cell. For a more detailed description of the method, the reader is referred to [8].

One key element in the zonal RANS-LES method is the generation of a physically meaningful inflow for the LES satisfying the underlying conservation equations. All turbulent quantities predicted by the RANS turbulence model need to be transferred into resolved large scale eddies carrying the turbulent kinetic energy and moments as predicted by the upstream RANS solution. This is accomplished by the RSTG method by Roidl et al. [18]. From the RANS solution, virtual eddy cores are determined and injected at the RANS–LES interface and their induced velocity fluctuations at the inlet plane are superimposed to the mean flow field defined by the RANS solution.

4. Computational Setup

The computational methodology from Section 3 is used to analyse three configurations of a NACA 0012 aerofoil, the first, baseline configuration has a standard solid and thin trailing edge to avoid any bluntness noise, the second is equipped with a rectangular porous trailing edge, and the third has a poro-serrated trailing edge, where the serrations are filled by a porous material, see Figure 1 (left).

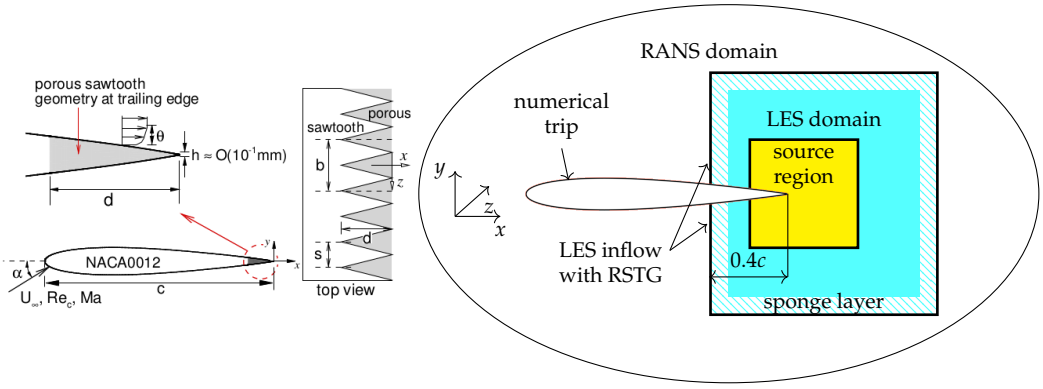


Figure 1. Schematic of the poro-serrated TE with b = d = 0.15c (**left**) and schematic of the RANS and the LES domains around the NACA 0012 aerofoil including the acoustic source region (**right**).

The focus is on the analysis of the turbulent, unsteady flow field. At the given conditions, the flow remains attached such that we take advantage of a computationally efficient zonal approach, in which the RANS equations are solved in the entire domain first, followed by an LES limited to the trailing edge region, which is fully embedded inside the RANS domain. It starts at 0.6*c* to allow the turbulent boundary layer to fully develop to a physically correct state before advecting over the porous surface. The overall RANS–LES setup is sketched in Figure 1 (right).

The simulations are conducted for a uniform flow at a Mach number of $M = 0.1118$, a Reynolds number of $Re = 1.0 \times 10^6$ and an angle of attack of $\alpha = 0°$. The RANS equations are solved on a two-dimensional structured multi-block mesh of O-type with a finite trailing edge thickness of 0.26%c. A mesh with 860×10^3 cells in the fluid domain outside of the aerofoil and, for the porous case, 7×10^3 cells in the porous trailing edge, is used. The mesh extends 50c away from the aerofoil and the finest resolution in inner coordinates in the wall-normal direction is $\Delta y^+_{wall,FP} < 1$ at the solid wall or the fluid–porous (FP) interface. In the streamwise direction, the cells are clustered near the trailing edge and near the transition from the solid boundary to the FP-interface with a minimum spacing of $\Delta x^+ \approx 10\Delta y^+_{wall,FP}$. Figure 2 (left) shows a magnification of the trailing edge region.

The mesh for the solid setup was derived from the porous mesh by making as few changes as possible to exclude any impact on the comparison due to the mesh.

The fully embedded LES domain covers the last 40% of the aerofoil and extends 3.5c into the wake, 3c in the flow-normal direction and 0.15c in the spanwise direction to capture two periods of the serrations. The mesh is locally refined near the aerofoil wall and the FP-interface with a minimum isotropic grid spacing of $\Delta^+ < 5$, which results in a total of 407×10^6–467×10^6 cells, where the latter also includes the cells inside the discretised porous material. A snapshot of such a mesh is given in Figure 2 (right). The LES domain is surrounded by a sponge layer to absorb reflections generated by eddies leaving the domain and to smoothly impose the far-field conditions obtained from the RANS solution. At the inflow, only a sponge layer controlling the pressure is applied to minimise spurious noise resulting from the RSTG. The LES is initialised with the mean flow field obtained from the RANS solution to shorten the transient phase. In the spanwise direction, periodic boundary conditions are applied.

The porous material starts at a chord length of 85% of the NACA 0012 aerofoil to allow for a redistribution of the near-wall turbulent structures before passing over the trailing edge. A homogeneous and isotropic porous material, as proposed in [19], is assumed. The material parameters are calibrated in [20] for use in the Darcy–Forchheimer model and are $\varphi = 0.986$, $Da = 1.325 \times 10^{-8}$ based on the aerofoil chord and $c_F = 0.0$, due to a lack of calibration data.

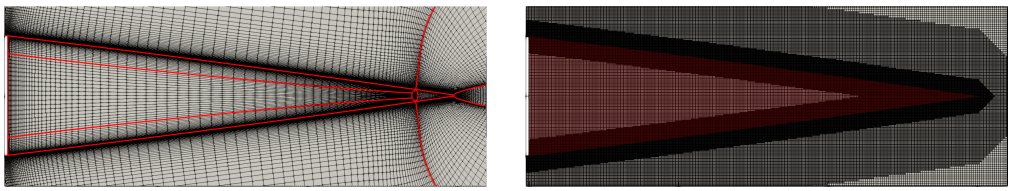


Figure 2. Detailed views of the structured RANS mesh (**left**) and the unstructured Cartesian mesh of the LES (**right**) for the porous configuration. The red shadowed area in the right figure indicates the porous region.

5. Data Processing

First, the temporal convergence of the LES towards a statistically stationary solution is investigated in Figure 3 by plotting the evolutions of the absolute errors of the local mean streamwise velocity $\varepsilon_{\overline{u}}$ and the Reynolds shear stress $\varepsilon_{\overline{u'v'}}$ at $x/c = 0.0038$ and $y^+ = 20$ inside the boundary layer, to capture the convected turbulence from downstream of the RSTG treatment. It is most convenient for the assessment of convergence to use a deterministic measure, which quickly adapts within a short time history. Hence, spatial averaging to obtain statistics is preferred over time averaging. Using the axisymmetry with respect to the xz-plane, samples from the upper and lower side are averaged, where $\overline{u'v'}|_y = -\overline{u'v'}|_{-y}$, as is the data in the spanwise direction in the case of the solid and the straight porous TE, due to spanwise homogeneity. Additionally, a moving average over $tU_\infty/c = 1.17$ to obtain statistically converged data is exemplarily overlayed in Figure 3 for the rectangular porous TE. Following this metric, the first $tU_\infty/c = 1.82$ time units have been considered as transitional from the initial RANS solution towards the scale resolving LES flow field and are discarded from the following analysis. Data were recorded for the last $T_s = 4.81c/U_\infty$, corresponding to 10 cycles at 196 Hz.

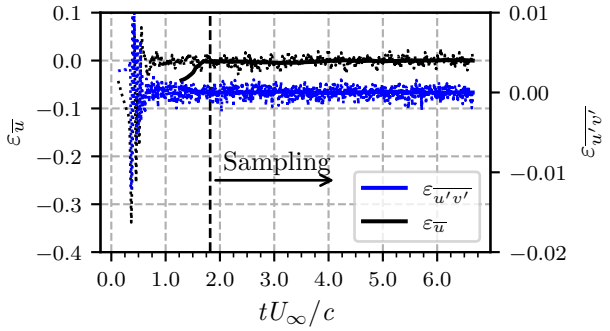


Figure 3. Temporal evolutions of the local mean streamwise velocity and the Reynolds shear stress near the TE over the non-dimensional time.

6. Results

In Figure 4, a snapshot of the vortical structures of the flow around the poro-serrated trailing edge is shown by isocontours of the Q-criterion colour coded by the local Mach number. The RSTG is clearly able to promote the formation of 3D flow features of various scales immediately downstream of the inflow plane, which are convected downstream. Unlike the solid and the porous configurations, the poro-serrated aerofoil will cause an inhomogeneous flow field in the spanwise direction on scales, which are of interest for the current work, and hence in the remainder the flow field will be analysed in xy-planes through the tip of a serration and a root.

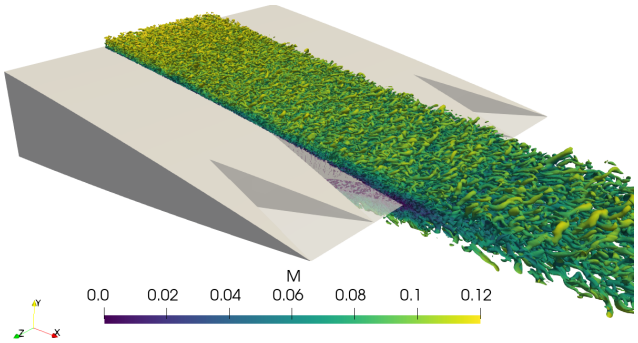


Figure 4. Visualization of vortical structures by the instantaneous isosurfaces of the Q-criterion colour coded by the Mach number for the flow around the poro-serrated TE.

The c_p- and c_f-distributions along the last 40% of the chord are compared in Figure 5 for the solid and porous trailing edges. Towards the trailing edge, the porous treatment slightly affects the pressure recovery and is most pronounced for the fully porous TE. This is in agreement with the stronger boundary layer growth over the porous surface, which is also confirmed by the integral boundary layer parameters discussed later. Note that the c_p distribution of the porous TE has a small plateau at the beginning of the porous surface, where the pressure recovery is interrupted shortly, as is typical for a locally excessively growing boundary layer. This effect might be relevant for a poro-serrated TE for larger sawtooth periods b, and hence a larger serration opening angle. The c_f distributions exhibit a sharp increase up to a chord length of about $x/c = -0.35$, which reflects the transition to a turbulent boundary layer state. Note that the total wall-shear stress at a porous surface is defined as the sum of the viscous $\tau_{w,v}$ and the Reynolds-shear stress as:

$$\tau_w = \tau_{w,v} - \overline{\rho u' v'}|_{y_w}, \tag{11}$$

since the fluid velocity does not vanish at the porous surface. For ease of notation, u' and v' are meant to be the local streamwise and wall-normal velocity components, numerically evaluated on the fluid side Ω_f of the cut fluid–porous cell. Similarly, appropriate definitions

for the friction velocity and a length scale can be formulated based on Equation (11). For the porous and the poro-serrated TE in the root plane, the viscous wall shear-stress $\tau_{w,v}$ is plotted separately. It is evident that the total stress is dominated by the unsteady momentum transfer caused by the fluctuating velocity field through the permeable wall, which is in accordance with other observations in the literature [10]. An initial spike is followed by a gradual decay to a value well above the solid case. In the tip planes of the poro-serrated trailing edge, the c_f distributions agree with the solid baseline case. The spanwise variation of the friction coefficient is illustrated in Figure 6. The highest values occur at the edges of the serrations. As will also be apparent in the subsequent analysis, the porous treatment at the current flow conditions has only a local effect on the one-point statistics, i.e., the flow encountered over the solid part of the serrations resembles the flow over a pure solid TE.

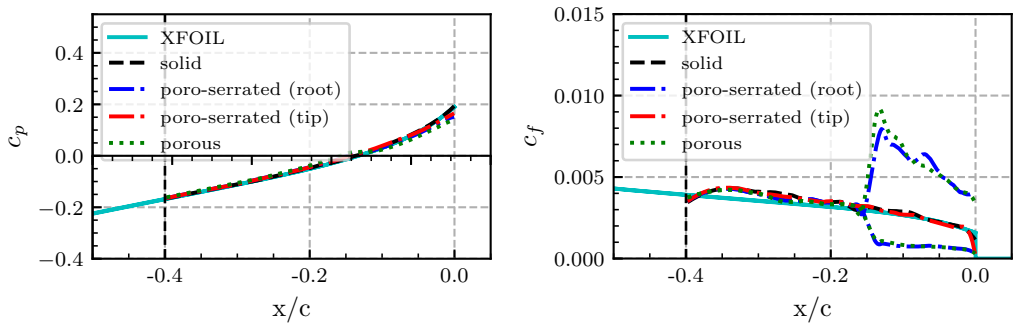


Figure 5. Distributions of c_p (**left**) and c_f (**right**) plotted against XFOIL [21] predictions. Dashed line indicates the inflow plane of the LES domain.

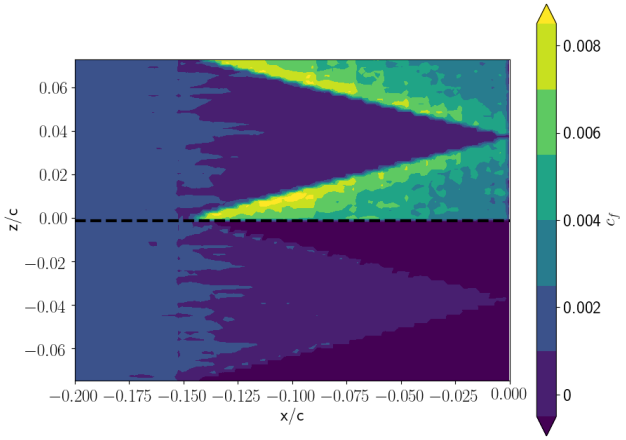


Figure 6. Contours of the total shear stress Equation (11) (**top**) and the viscous shear stress contribution (**bottom**) on the poro-serrated trailing edge.

In Figure 7, contour plots of the mean streamwise velocity $\overline{u}$ and the mean turbulent kinetic energy k in xy-planes near the trailing edge are shown. The velocity distribution in the tip plane of the poro-serrated TE is almost identical to that of the solid case, and likewise the distribution in the root plane resembles the rectangular porous TE case. Even though the velocities inside the porous material are negligible on scales of the outer mean flow, streamlines show a weak counter rotating pair of vortices forming downstream of the solid material. Near the solid–fluid transition at $x/c = -0.15$, the streamlines indicate a slightly more disordered movement for the rectangular porous TE, not shown here. The k-distribution in the tip plane is very similar to the one of the solid TE. In the root plane, the turbulence intensity is up to 32% higher. Visually, the high turbulence intensity region originates at $x/c = -0.15$ and extends in the downstream direction. In the spanwise direction, these regions periodically repeat and are confined to the porous surface part of the serrations.

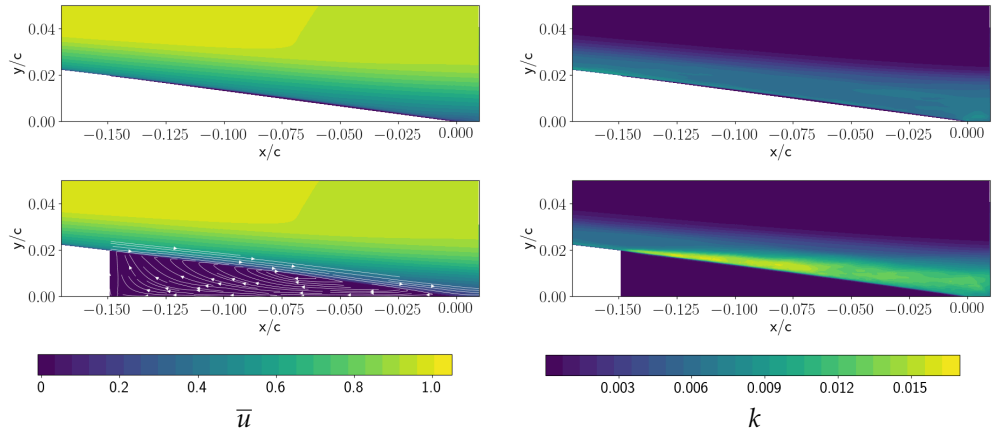


Figure 7. Mean streamwise velocity (**left**) and turbulent kinetic energy (**right**) contours in tip (**top**) and root (**bottom**) planes.

A more quantitative analysis is presented in Figure 8 by wall normal profiles of the mean streamwise velocity, mean turbulent kinetic energy, and streamwise and wall-normal Reynolds stress components at $x/c = \{-0.15, -0.1\}$. The wall-normal coordinate is non-dimensionalised by the momentum thicknesses of the individual solutions. The values are given in Table 1 at the same streamwise positions, where also other integral boundary layer parameters are summarised. They are calculated following the instructions from the BANC II workshop on how to obtain the boundary layer thickness and the free-stream velocity. At the most upstream location, where the wall is impermeable in all cases, the velocity profiles are similar and exhibit the typical law of the wall behaviour of a turbulent boundary layer, when plotted in inner scales. The fluctuating velocity field is dominated by $\overline{u'u'}$ close to the wall with a very sharp peak nearly four times higher than $(\overline{v'v'})_{max}$. This is characteristic for the two-component turbulence in wall bounded flows, where $\overline{u'u'} \propto y^2$ as opposed to $\overline{v'v'} \propto y^4$. Minor differences are visible in root planes for the poro-serrated TE, but overall the upstream impact of the porous surface is limited. Further downstream, at $x/c = -0.1$ the profiles diverge, where the profiles over a solid surface point have similarities and likewise the two distributions over a permeable point. Despite similar boundary layer thicknesses, e.g., δ_{99}, over a porous surface the profiles deviate from the law of the wall and exhibit a momentum deficit, which is also reflected in the displacement δ_1 and momentum thicknesses δ_2, both being larger. The mean and the fluctuating velocities are non-zero at the fluid–porous interface and decay towards zero inside the porous material. The distinct peak in $\overline{u'u'}$ resulting from the streamwise oriented near wall structures diffuses away from the wall to form a larger wall-normal region of high turbulence intensity over the porous surface. This behaviour translates into the distribution of k. The shift of the maximum away from the wall can be explained by considering the wall normal Reynolds stress $\overline{v'v'}$, the maximum of which has almost doubled. It is this relaxed form of the no-penetration boundary condition on a macroscopic scale over a porous surface, which intensifies the wall normal turbulent convection $\overline{u'_y u'_i u'_j}$, leading to a more rapid boundary layer growth. This triple correlation converges slowly and is not shown here. The permeability Reynolds number $Re_\kappa = \frac{\sqrt{\kappa} u_{w,\tau}}{\nu}$, where the friction velocity $u_{w,\tau}$ is determined by the total shear stress Equation (11) at the fluid–porous interface, is a measure for how permeable the wall is. Note that in [10] $Re_\kappa = 9.35$ is already considered as highly permeable. With $Re_\kappa \in (44, 61)$ at the probing points (cf. Table 1) the current porous media can be classified as highly permeable. At the trailing edge similar tendencies can be observed.

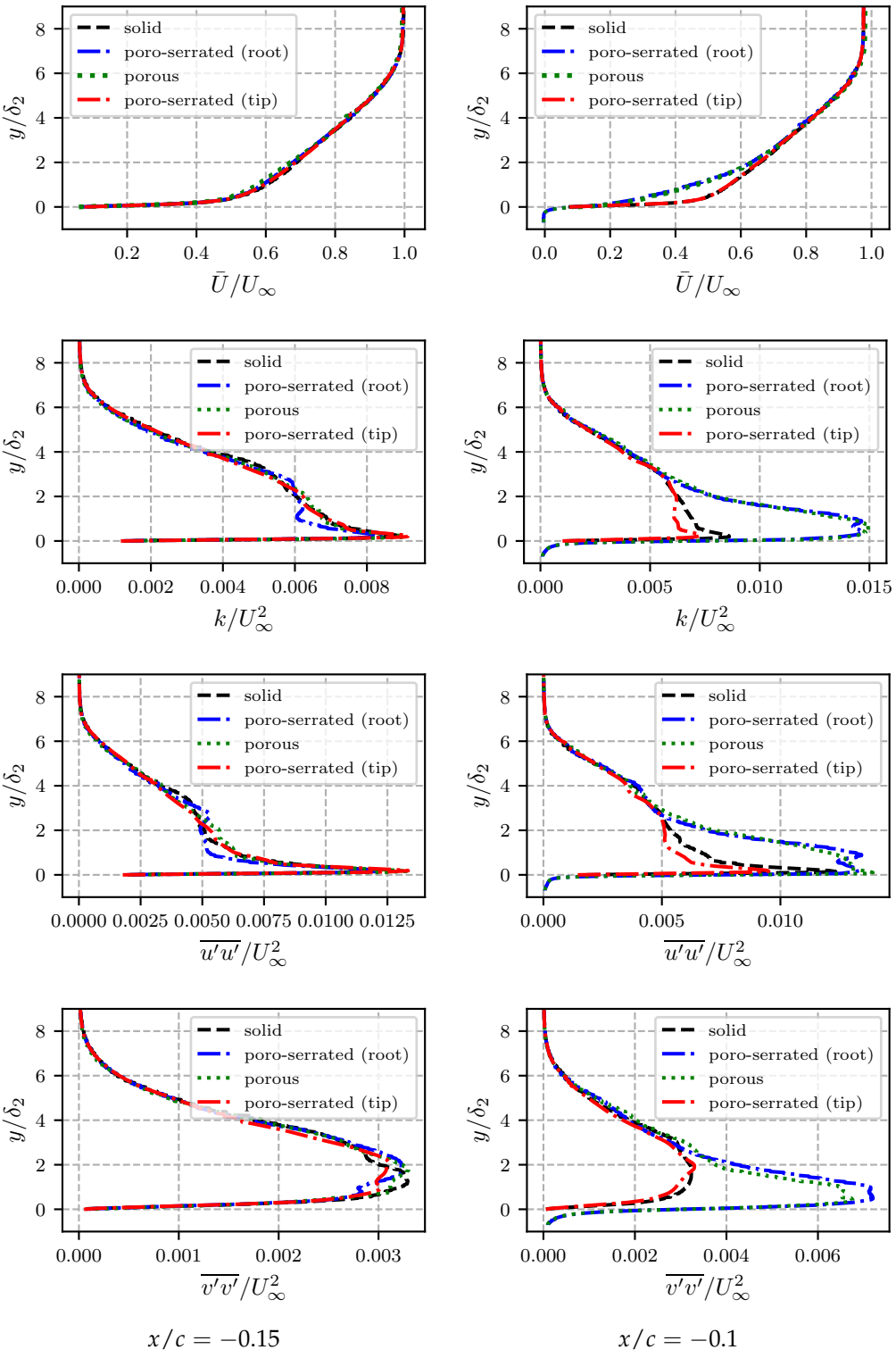


Figure 8. Wall-normal profiles of the mean streamwise velocity, turbulent kinetic energy, and the streamwise and wall-normal Reynolds stresses.

Table 1. Boundary layer parameters at three streamwise positions along the airfoil. The quantities are the displacement thickness δ_1, the momentum thickness δ_2, the shape factor H_{12}, and the permeability Reynolds number Re_κ.

	Solid			**Porous**			**Poro-Serrated (Root)**			**Poro-Serrated (Tip)**		
x/c	-0.15	-0.1	0.0	-0.15	-0.1	0.0	-0.15	-0.1	0.0	-0.15	-0.1	0.0
δ_1 [mm]	1.52	1.74	2.98	1.6	2.08	3.7	1.57	2.06	3.59	1.55	1.79	3.04
δ_2 [mm]	0.99	1.11	1.62	1.02	1.16	1.69	1.0	1.14	1.65	1.0	1.14	1.67
H_{12} [-]	1.54	1.57	1.84	1.57	1.79	2.19	1.55	1.82	2.18	1.54	1.57	1.82
Re_κ [-]	0	0	-	50	61	-	44	59	-	0	0	0

The differences in the streamwise and wall-normal Reynolds stress components can be further analysed by the anisotropy invariant map introduced by Lumley & Newman [22] in Figure 9 at $x/c = -0.1$. It characterises the state of turbulence in the boundary layer by the second (II) and third (III) invariant of the normalised Reynolds stress anisotropy tensor $b_{ij} = \overline{u_i' u_j'}/2k - 1/3\delta_{ij}$ defined by $\mathrm{II} = 1/2 b_{ij} b_{ji}$ and $\mathrm{III} = 1/3 b_{ij} b_{jk} b_{kl}$. Note that the first invariant is zero by construction. The invariants are linked to the normal stresses of the symmetric Reynolds stress tensor expressed in the principal axes, and hence are well suited to characterise the dimensionality and symmetry properties of the local turbulence state.

When plotted in a II-III-plot all realisable turbulent states lie within the Lumley triangle defined by three limiting curves. Some characteristic points are the centre point at (0,0), which marks the state of isotropic turbulence, the point of isotropic two-component turbulence at the upper left (2C, iso), where turbulence is axisymmetric with equal magnitude fluctuations in a plane without directional preferences, and the one component turbulence at the top left not shown here for better illustration of the results. The connecting lines of these three states also define characteristic states, from which the straight line marked as '2C' defines the state of two-component flow as observed very near solid walls, where turbulent fluctuations are in planes parallel to the wall. In Figure 9 the states occurring when traversing from inside the porous material to $y^+ = 200$ are plotted. For orientation, markers are added to indicate certain distances from the wall and the state at the fluid–porous interface. The distributions at solid points start near the two-component limiting curve, as is typical for turbulent boundary layers, where $\overline{v'v'}/k \to 0$ for $y \to y_w$ and converge towards the isotropic state, when moving away from the wall. In contrast, the velocity components do not decay to zero over permeable walls and contribute substantially to k as already observed in Figure 8. Deep inside the porous material the model equations predict an isotropic decay of all components, i.e., without a directional preference. At the fluid–porous interface, however, all three eigenvalues of the Reynolds-stress tensor are non-zero.

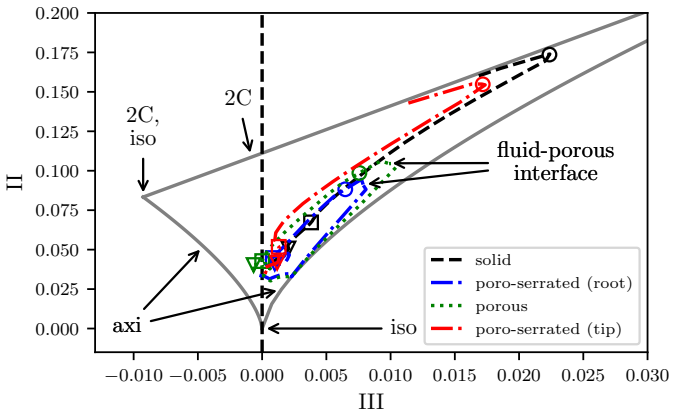


Figure 9. Anisotropy map at $x/c = -0.1$ with the distributions describing the turbulence state, when traversing from the solid wall or inside the porous medium to $y^+ = 200$. Markers indicate the distances $y^+ = 7$ (○), $y^+ = 50$ (□) and $y^+ = 100$ (▽) from the wall.

Next, the spectral content of the turbulence in the near wake at $x/c = 0.0025$ on the centreline is shown by the one-point frequency spectrum of the (isotropic) turbulent kinetic energy non-dimensionalised by the turbulent kinetic energy of the solid solution k_s in Figure 10. All four spectra exhibit a -5/3-power law behaviour over a substantial frequency range, which indicates that the present mesh resolution is able to capture part of the inertial subrange. For lower frequencies the spectral distribution downstream of the aerofoil in the tip plane of the poro-serrated TE is closer to that of the solid TE, while the solution in the root plane is closer to that of the pure porous TE, similar to the observations made above the aerofoil about the turbulent state, being only dependent on the local aerofoil surface. For frequencies St > 10, the solid solution has the least amount of energy in the smaller scales, while both poro-serrated distributions resemble each other, in particular in the inertial subrange. This indicates that the kinetic energy distribution of these structures with smaller timescales is more homogeneous in the spanwise direction. Towards higher frequencies, differentiability conditions on the velocity field require the spectrum to decay exponentially.

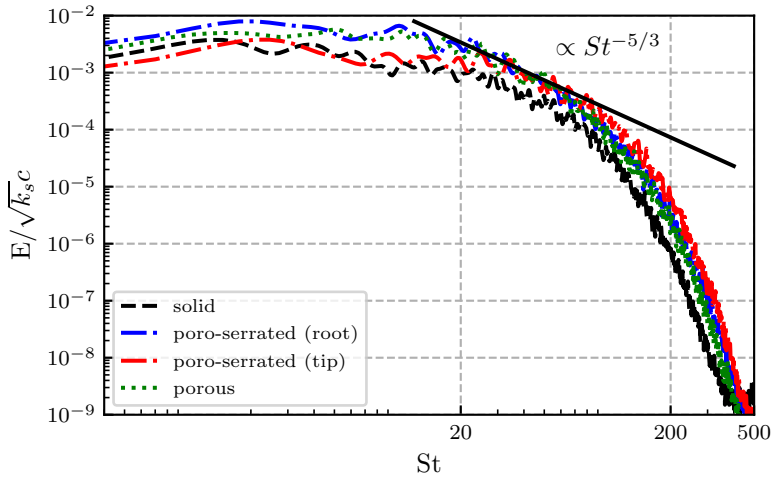


Figure 10. Frequency power spectral density of turbulent kinetic energy k at $x/c = 0.0025$ on the centreline.

The coherent structures can be investigated by means of two-point correlations. The normalised velocity correlation is defined as:

$$R_{ij}(\underline{x}, \underline{r}) = \frac{\langle u_i'(\underline{x}, t) u_j'(\underline{x} + \underline{r}, t) \rangle}{\langle u_i'(\underline{x}, t) \rangle^{1/2} \langle u_j'(\underline{x} + \underline{r}, t) \rangle^{1/2}}, \tag{12}$$

where utilising the ergodicity principle, the averaging is carried out in time. In Figure 11 longitudinal R_{22} and transversal R_{11} autocorrelation coefficients for separation distances in the vertical direction from the centreline are plotted. Note that the resulting integral correlation length scales are important parameters, which enter acoustic prediction models. From the centre point, the correlations downstream of the solid serration tip and the pure solid aerofoil, decline slightly faster indicating smaller structures in accordance to the boundary layer thicknesses. The R_{11} distributions exhibit larger differences between being downstream of a solid surface or porous medium. Both, for the solid and in the tip plane of the poro-serrated TE, the curves initially decay faster, but for larger separation distances slowly approach a state of zero correlation. Downstream of the porous material the coherence shows a more distinct behaviour typical for clearly defined closed regions of strong coherence, with the poro-serrated root curve showing a minimum and therefore an anti-correlation at $y/c = 0.01$.

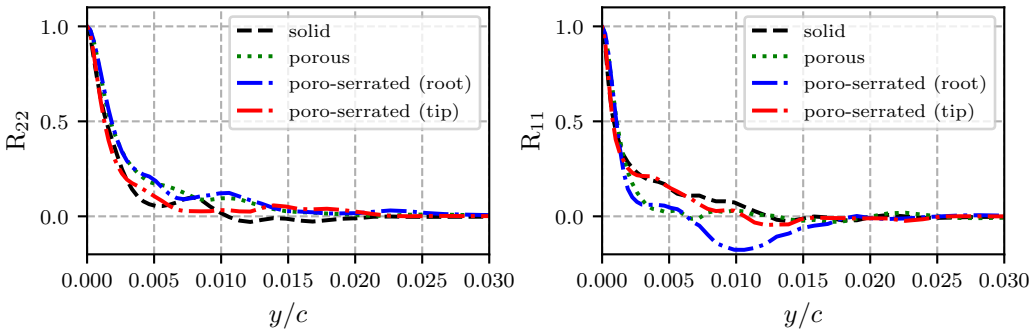


Figure 11. Autocorrelation functions of the wall-normal (**left**) and streamwise (**right**) velocity fluctuations with separation distances from the centreline in the normal direction at $x/c = 0.0038$.

7. Conclusions

In the present study, the turbulent flow fields around NACA 0012 aerofoils with a solid TE, a porous TE and a poro-serrated TE, have been investigated. Computationally efficient zonal RANS-LES simulations have been performed, where both system of equations have been augmented to take the flow over and through porous surfaces macroscopically into account. The investigation of the turbulence in the TE region revealed an increased turbulence intensity and a thickening of the boundary layer over porous surfaces by an increase in turbulent convection normal to the wall. The relaxed kinematic boundary condition alters the Reynolds stress tensor towards a more isotropic state. Streamwise fluctuations are redistributed in favour of wall normal fluctuations. For the geometrical arrangement and flow condition considered in the current work, the porous surface has had only a local impact on the statistical moments of first and second orders. Experiments and numerical simulations have revealed a noise mitigation potential of porous treatments, but in accordance with the literature, the current findings suggest an increase in hydrodynamic fluctuations inside the faster growing turbulent boundary layer. The effects of lift by a variation of the angle-of-attack are another key point of interest, which needs to be addressed. This also raises the question of the feasibility of the zonal technique.

Author Contributions: Writing—original draft preparation, S.S. and M.M.; writing—review and editing, S.S.; supervision, M.M. and W.S. All authors have read and agreed to the published version of the manuscript.

Funding: This research was funded by the Deutsche Forschungsgemeinschaft DFG grant number SCHR 309/54.

Data Availability Statement: The data presented in this study are available on request from the corresponding author.

Acknowledgments: The support of this research by the Deutsche Forschungsgemeinschaft DFG under grant SCHR 309/54 is gratefully acknowledged. The authors also gratefully acknowledge the Gauss Centre for Supercomputing e.V. (www.gauss-centre.eu, accessed on 15 December 2021) for funding this project by providing computing time on the GCS Supercomputer HAWK at Höchstleistungs-Rechenzentrum Stuttgart (www.hlrs.de, accessed on 15 December 2021).

Conflicts of Interest: The authors declare no conflict of interest.

References

1. Teruna, C.; Avallone, F.; Casalino, D.; Ragni, D. Numerical investigation of leading edge noise reduction on a rod-airfoil configuration using porous materials and serrations. *J. Sound Vibr.* **2021**, *494*, 115880. [CrossRef]
2. Geyer, T.; Sarradj, E. Trailing Edge Noise of Partially Porous Airfoils. In Proceedings of the 20th AIAA/CEAS Aeroacoustics Conference, Atlanta, GA, USA, 16–20 June 2014. [CrossRef]
3. Sarradj, E.; Geyer, T. Noise Generation by Porous Airfoils. In Proceedings of the 13th AIAA/CEAS Aeroacoustics Conference (28th AIAA Aeroacoustics Conference), Rome, Italy, 21–23 May 2007. [CrossRef]
4. Zamponi, R.; Satcunanathan, S.; Moreau, S.; Ragni, D.; Meinke, M.; Schröder, W.; Schram, C. On the role of turbulence distortion on leading-edge noise reduction by means of porosity. *J. Sound Vib.* **2020**, *485*, 115561. [CrossRef]

5. Koh, S.R.; Zhou, B.; Meinke, M.; Gauger, N.; Schröder, W. Numerical analysis of the impact of variable porosity on trailing-edge noise. *Comput. Fluids* **2018**, *167*, 66–81. [CrossRef]
6. Whitaker, S. *Theory and Applications of Transport in Porous Media: The Method of Volume Averaging*; Kluwer Academic: London, UK, 1999.
7. Koh, S.R.; Meinke, M.; Schröder, W. Numerical analysis of the impact of permeability on trailing-edge noise. *J. Sound Vib.* **2018**, *421*, 348–376. [CrossRef]
8. Satcunanathan, S.; Meinke, M.H.; Schröder, W. Prediction of Noise Mitigation by Porous Media based on a Direct-Hybrid CFD/CAA Method. In Proceedings of the 25th AIAA/CEAS Aeroacoustics Conference, Delft, The Netherlands, 20–23 May 2019. [CrossRef]
9. Mößner, M.; Radespiel, R. Modelling of turbulent flow over porous media using a volume averaging approach and a Reynolds stress model. *Comput. Fluids* **2015**, *108*, 25–42. [CrossRef]
10. Breugem, W.; Boersma, B.; Uittenbogaard, R. The influence of wall permeability on turbulent channel flow. *J. Fluid Mech.* **2006**, *562*, 35–72. [CrossRef]
11. Satcunanathan, S.; Meinke, M.; Schröder, W. Numerical Investigation of a Porous Trailing Edge by a Zonal RANS/LES Simulation. In *STAB/DGLR Symposium*; Springer: Cham, Switzerland, 2020; pp. 666–676.
12. Whitaker, S. Flow in Porous Media I: A Theoretical Derivation of Darcy's Law. *Transp. Porous Med.* **1986**, *1*, 3–25. [CrossRef]
13. Whitaker, S. The Forchheimer equation: A theoretical development. *Transp. Porous Med.* **1996**, *25*, 27–61. [CrossRef]
14. Breugem, W.P. The Influence of Wall Permeability on Laminar and Turbulent Flows: Theory and Simulations. Ph.D. Thesis, TU Delft, Delft, The Netherlands, 2005.
15. Chien, K.Y. Predictions of channel and boundary-layer flows with a low-Reynolds-number turbulence model. *AIAA J.* **1982**, *20*, 33–38. [CrossRef]
16. Schneiders, L.; Hartmann, D.; Meinke, M.; Schröder, W. An accurate moving boundary formulation in cut-cell methods. *J. Comput. Phys.* **2013**, *235*, 786–809. [CrossRef]
17. Jameson, A. Solution of the Euler equations for two dimensional transonic flow by a multigrid method. *Appl. Math. Comp.* **1983**, *13*, 327–355. [CrossRef]
18. Roidl, B.; Meinke, M.; Schröder, W. A Reformulated Synthetic Turbulence Generation Method for a Zonal RANS-LES Method and its Application to Zero-Pressure Gradient Boundary Layers. *Int. J. Heat Fluid Flow* **2013**, *44*, 28–40. [CrossRef]
19. Zamponi, R.; Van de Wyer, N.; Schram, C.F. Experimental investigation of airfoil turbulence-impingement noise reduction using porous treatment. In Proceedings of the 25th AIAA/CEAS Aeroacoustics Conference, Delft, The Netherlands, 20–23 May 2019. [CrossRef]
20. Satcunanathan, S.; Zamponi, R.; Meinke, M.; Van de Wyer, N.; Schram, C.; Schröder, W. Validation of a model for acoustic absorption in porous media. In Proceedings of the 48th International Congress and Exhibition on Noise Control Engineering, Madrid, Spain, 16–19 June 2019.
21. Drela, M. XFOIL: An analysis and design system for low Reynolds number airfoils. In *Low Reynolds Number Aerodynamics*; Springer: Berlin/Heidelberg, Germany, 1989; pp. 1–12.
22. Lumley, J.L. Computational modeling of turbulent flows. *Adv. Appl. Mech.* **1979**, *18*, 123–176. [CrossRef]